Comparison of Gas Velocity Measurements and CFD Predictions in the Exhaust Duct of a Stationary Source

Rodney Bryant, Olatunde Sanni, Elizabeth Moore, R. Paul Borthwick, Marco Fernandez, Iosif Shinder, Jiann Yang, and Aaron Johnson

National Institute of Standards and Technology
Gaithersburg, MD 20899

ABSTRACT

Two series of independent flow measurements were conducted for cross validation of flow velocity in the exhaust duct of the NIST Large Fire Laboratory. In the first series, two pressure measurement probe types, an S probe and a 3-D probe, were used to perform velocity profiling across two chords of the exhaust duct. Several detailed velocity profiles were generated using a probe traverse spacing of 2.54 cm (1.0 in). CFD simulations showed good qualitative agreement with measurements for cold flow conditions. The second series of measurements used two S probes, one on each chord, and a minimum of 20 EPA Method 1 traverse positions per chord. Qualitative comparisons of the velocity profiles showed that the flow profiles at the sampling plane were sensitive to run conditions such as flow inlet location, flow magnitude, and heat content of the flow.

INTRODUCTION

Greenhouse gas emissions mitigation approaches are heavily reliant on accurate determination of the mass flow rate measurement at or near the source. Many industrial continuous emissions monitoring (CEM) methods for greenhouse gases are based on gas species concentration measurements along with a total flow measurement. Large uncertainties in either measurement result in greater uncertainty in reported total emissions. Emission determinations having large uncertainty make it difficult to judge whether emission targets are being met locally - at the source, within a region, and ultimately throughout the world.

Emission measurements in the NIST Large Fire Laboratory (LFL) are made in the exhaust duct, upstream of its pollution abatement system. Previous experimental and computational results suggested that the flow in the exhaust duct could be sensitive to the flow path and origin (*i.e.* any one of the three exhaust hoods). The exhaust duct velocity is measured with an averaging pitot tube (annubar[1]). The device is not capable of providing flow profile information. In this work, the annubar measurement was conducted alongside two independent velocity measurements made with 1) an S probe and 2) a 3-D probe, both calibrated in the NIST wind

[1] Throughout this document certain commercial equipment, instruments, or materials are identified to foster understanding. Such identification does not imply recommendation or endorsement by the National Institute of Standards and Technology, nor does it imply that the materials or equipment identified are necessarily the best available for the purpose.

tunnel. The S probe and 3-D probe were used to measure the velocity profile in the exhaust duct along two orthogonal chords spanning the diameter, D = 1.50 m (5 ft).

In the present comparison, a natural-gas burner under steady-state conditions was used as the emissions source. To establish a measurement baseline, velocity traverses using the S probe and 3-D probe were first conducted without the natural-gas burner (*i.e.*,cold flow conditions). Subsequent measurements were conducted with the burner for various inlet conditions (*e.g.*, exhaust hood, heat content, burner location and flow magnitudes) to simulate normal operational changes.

The velocity field was also calculated using computational fluid dynamics (CFD). The accuracy of the computed velocity field was assessed via comparison to the chordal velocity profiles measured by the S probe and 3-D probe. The CFD calculations modeled only the cold flow conditions when the large hood was used. The following sections present a description of the experimental and numerical procedures and discussion of the results.

FACILITY DESCRIPTION

The NIST Large Fire Laboratory is a large-scale facility for the study of a broad range of fire phenomena, including the burning of materials, products, furnished rooms, and portions of buildings.[1] The primary measurement of the facility is the transient heat release rate or the amount of power generated from the burning of materials. The facility is equipped with the three exhaust hoods shown in Figure 1a including a large hood with dimensions of 9 m × 12 m, a medium hood with dimensions of 6 m × 6 m, and a small hood with dimensions 3 m × 3 m. The largest hood can remove the effluent of fires at a rate of up to 2690 m^3/min. This allows for the removal of effluents for fires with heat release of up to 10 MW. Sustained periods of burning are possible for heat release of 3 MW or less; fires greater than 3 MW are run for short durations.

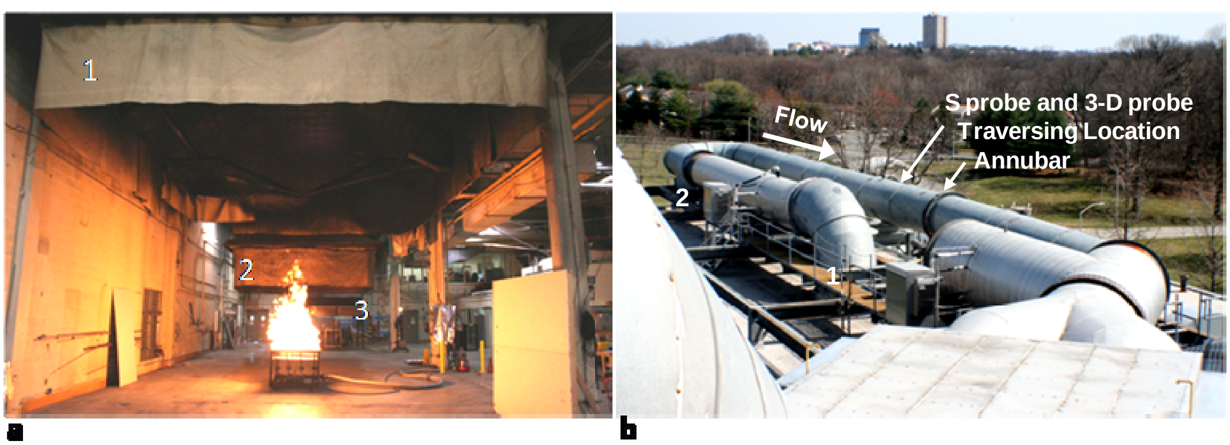

Figure 1. a) Natural-gas burner under the largest of three exhaust hoods (#1-Large 9 m × 12 m, #2- Medium 6 m × 6 m, #3-Small 3 m × 3 m); b) Portion of the exhaust duct on the roof of the facility and prior to the pollution control system.

The exhaust duct, shown in Figure 1b, runs horizontally along the roof of the facility with a series of turns. The labels 1 and 2 in Figure 1b show the locations where effluents from the large hood and medium hood, respectively, enter the exhaust duct. As shown in the figure, the annubar was installed downstream of the measurement plane traversed by the S probe and 3-D probe. The inner diameter of the exhaust duct at the measurement plane is $D = 1.50$ m ± 0.06 m. The measurement plane was located 9.17 D downstream of the 180° bend in the exhaust pipe and the annubar was positioned 2 D downstream of the measurement plane.

COMPUTATIONAL METHODS

The CFD model solves the steady, three-dimensional Navier-Stokes and continuity equations using the finite volume method [2]. In this method, fluxes of momentum and mass are conserved on finite volumes rather than on the differential volumes of the governing partial differential equations (*i.e.*, Navier-Stokes and continuity equations). Consequently, on each finite volume in the computational domain, the partial differential equations are converted into a coupled set of non-linear algebraic equations. Iterative techniques are used to solve this system of algebraic equations over the entire computational domain. Iterations are continued until the residuals (*i.e.*, error in the numerical solutions) are reduced by 6 orders of magnitude. The computational domain used to model the large burner and exhaust ducting consisted of 822,835 finite volumes. The mesh is shown in Figure 2. Although the mesh includes the pipe section that connects to the medium hood, the large hood was the source for flow for all of the CFD simulations. Computations were also performed using coarser grids, with no discernible difference in velocity profiles, thereby establishing the grid independence of the solution.

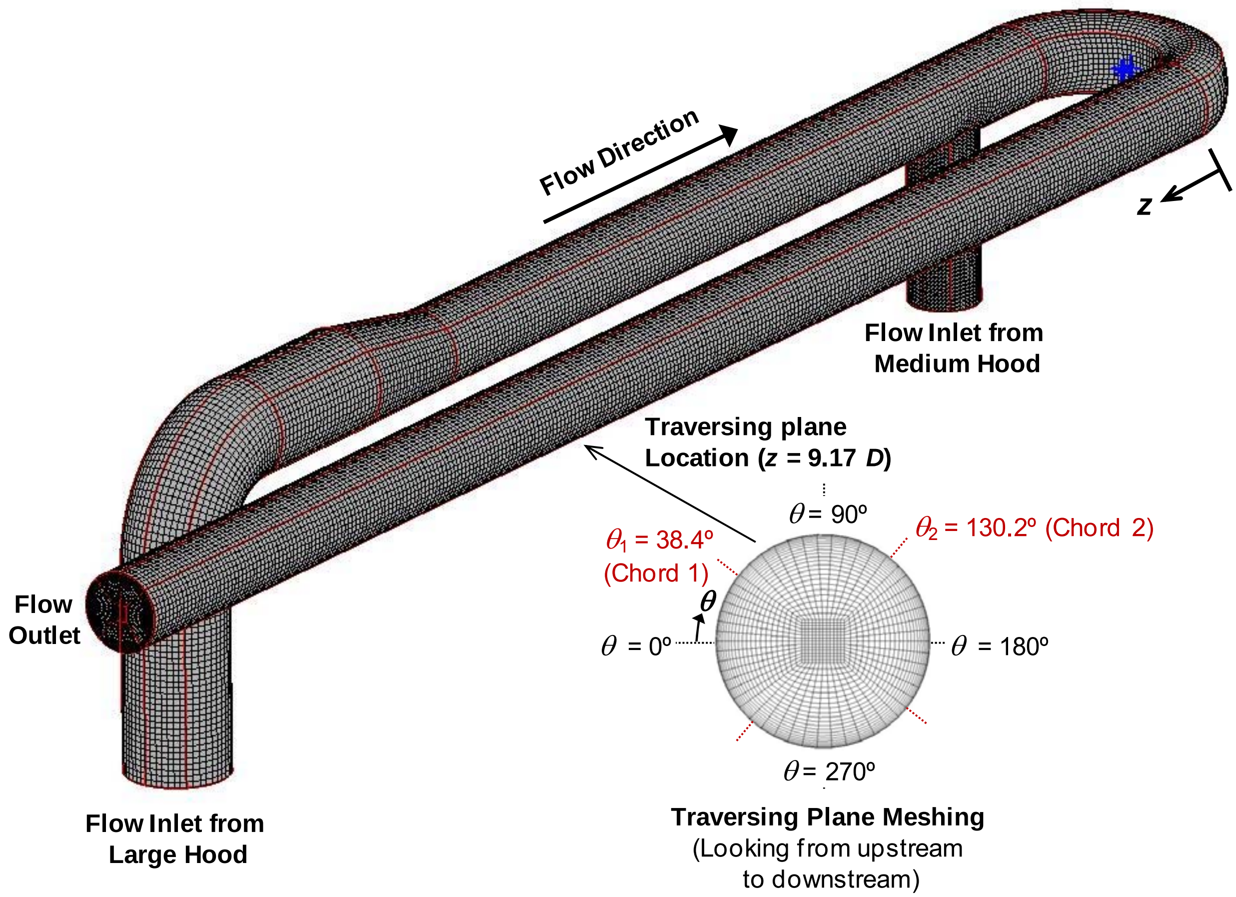

Figure 2. CFD mesh showing the geometry of the exhaust duct and the location of the traversing plane relative to the 180° bend in the duct.

The inlet flow boundary condition was set equal to the experimentally measured mass flow, while at the exit, atmospheric pressure conditions were specified. The flow computations were performed assuming the gas was both incompressible and isothermal with a constant temperature of $T = 297$ K. Turbulence was modeled using the Kato-Launder k-ϵ model since it accounts for regions of flow stagnation [3]. The inlet turbulence intensity was taken to be 2 %. As shown in Figure 2, the cross section of the mesh was clustered near the wall to account for the steep velocity gradients present in the boundary layer. The fine meshing near the wall ensures the validity of the wall functions used in the turbulent model.

The computations performed here used the commercial solver CFD-ACE. The output from the CFD model includes three-dimensional velocity vectors in each control volume of the grid. This facilitates comparison between the predicted and measured velocity profiles along chord 1 (at $\theta_1 = 38.4°$) and chord 2 (at $\theta_2 = 130.2°$). Moreover, the CFD model can be used to visualize advanced flow features (*e.g.*, recirculation zones, swirl decay, velocity profile development) that otherwise would require specialized experimental facilities. In the current work, the CFD indicated a recirculation zone just downstream of the 180° bend (see Figure 2) between $\theta = 0°$ and $\theta = 15°$. The asymmetric flow profile caused by the flow separation at $z = 0$ does not achieve a fully developed profile at the traversing plane just $z = 9.17\ D$ downstream from the bend. Consequently, the area-averaged velocity over the cross section cannot be completely determined by measuring the velocity at only two chords (*i.e.*, chords 1 and 2). However, the velocity field predicted by the CFD can be used to estimate this discretization error.

Figures 3a through 3f show the velocity profiles in the traversing plane along 12 diametric chords spaced 15° apart. In these figures, $\tilde{V}_\theta$ is the velocity along a diametric chord inclined at angle θ normalized by the area weighted velocity. The area weighted velocity is the mass flow divided by the cross sectional area and the average density. This normalization is used so that the average of N chordal velocities, $\left\langle \tilde{V}_\theta \right\rangle_N = \frac{1}{N}\sum_{n=1}^{N}\tilde{V}_{\theta,n}$, approaches the area weighted velocity as N increases. All of the 6 figures (*i.e.*, a through f) plot the velocity ($\tilde{V}_\theta$) along a diametric chord inclined at angle θ as well as the velocity ($\tilde{V}_{\theta+90°}$) along the perpendicular diametric chord. Based on these profiles, if traverses are done using only 2 orthogonal chords, the average chordal velocity, $\left\langle \tilde{V}_\theta \right\rangle_2$, will change as a function of θ. For example, traversing the measurement plane along the 2 chords, $\theta = 15°$ and $\theta = 105°$, yields a velocity that differs by 0.78 % from the velocity when traversed at $\theta = 30°$ and $\theta = 120°$. Twice the standard deviation (95 % confidence level) of the average velocities listed in Figures 3a through 3f, 0.96 %, is used to estimate the error that results from the discretization of the cross section into two diametric chords.

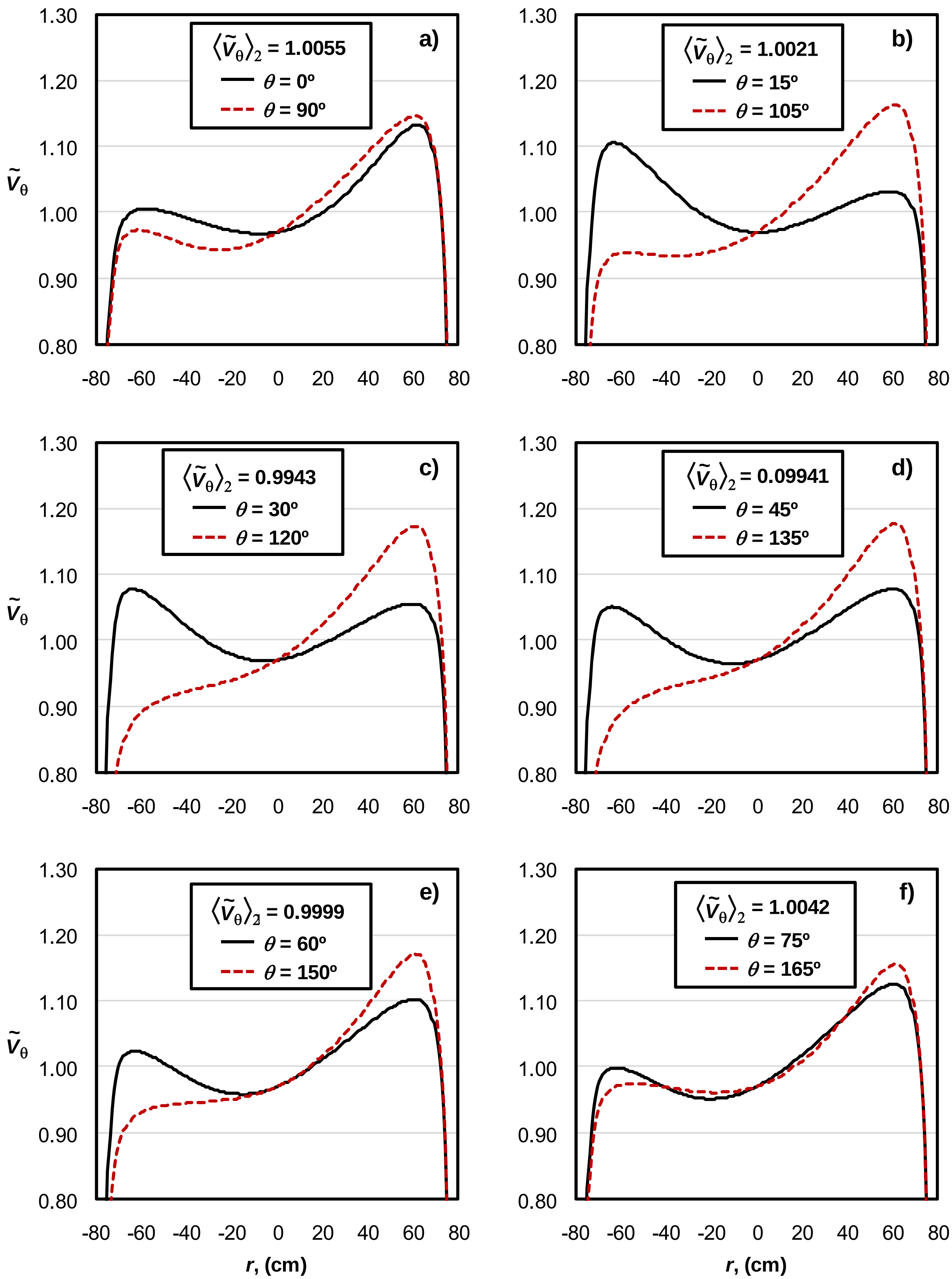

Figure 3. Computed velocities profiles in the traversing plane along 12 diametric chords spaced 15° apart.

EXPERIMENTAL METHODS

Velocity Profiling using S Probe and 3-D Probes

Two series of experiments were conducted to measure the velocity profile in the exhaust duct. Velocity profiles were measured on two perpendicular chords of the duct cross section for both series. In the first series, two pressure measurement probe types were used, S probe and 3-D probe. Each probe was equipped with a sensor for measuring gas temperature. The S probe was used to determine the near-axial velocity, therefore the velocity that accounts for the yaw angle of the flow. The 3-D probe was used to determine the axial velocity, therefore the velocity that accounts for the yaw and pitch angle. The S probe and the 3-D probe were interchanged between chords for the first level of cross validation of the velocity measurements.

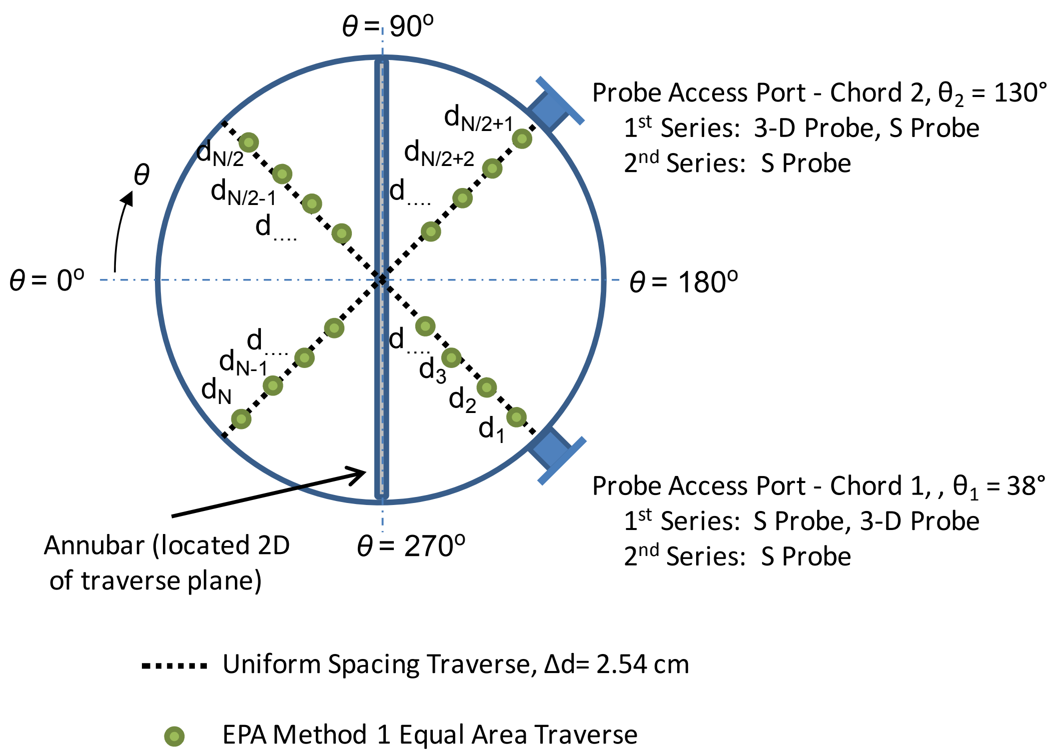

Figure 4. Cross-sectional view of velocity traverse plane for the horizontal exhaust duct and orientation of the annubar. (Viewed looking from upstream to downstream).

In the first series, 6 of the experiments were conducted with traverse spacing of 2.54 cm in order to fully characterize the velocity profile. The remaining 5 experiments in this series were conducted using 12 measurement positions that were within ± 1.00 cm of the equal area positions (due to time constraints the original markings at the 2.54 cm spacing were used) defined by EPA (Environmental Protection Agency) Method 1 [4]. The second series of experiments used two S probes, one on each chord. Measurement procedures followed EPA Method 2 [5] with 48 total traverse points (24 per chord) or EPA Method 2G [6] with 40 total traverse points (20 per chord). The choice of method depended on the amount of off-axis flow. Traverse points for this series corresponded to EPA Method 1 equal area positions. A schematic of the cross section for the velocity profiling measurements is shown in Figure 4. The figure shows that the two chords are nearly orthogonal with chord 1 located at θ_1 = 38° ± 1° and chord 2 at θ_2 = 130° ± 1°.

Velocity measurements were also made using an averaging pitot tube or annubar flowmeter. The annubar serves as the LFL's continuous flow monitoring device. It is mounted in a vertical orientation and positioned 2 diameters downstream of the velocity traverse plane. Average velocity measurements were recorded from the annubar for each velocity profiling experiment. The annubar was not disturbed during a series of experiments or between series. Therefore, the measurement provides a reference parameter for changes in experimental conditions.

RESULTS AND DISCUSSION

The flow traverses were conducted after steady-state conditions were achieved in the exhaust duct. Depending on the size of the fire, steady state could be reached in 20 min or less. Far less time was required to achieve steady state for cold flow experiments. Total test duration for the 2.54 cm spacing traverse was on the order of 1.5 h. Figure 5 demonstrates how the LFL was able to maintain steady conditions for the entire duration of an experiment. If necessary, the output of the burner and the speed of the exhaust fans could be adjusted to maintain steady conditions.

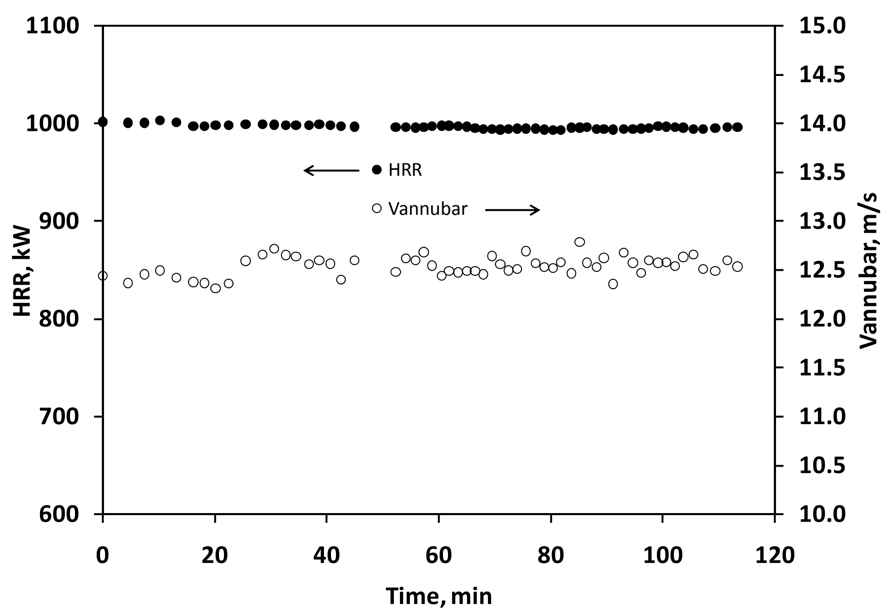

Figure 5. Example time history plots of heat release rate (HRR) from the natural-gas burner and gas velocity measured at the annubar over the duration of an experiment.

Measured Temperature Profiles and Yaw and Pitch Angles

Each velocity probe was configured with a thermocouple for gas temperature measurements and with a digital inclinometer to measure the yaw angle. Pitch angles were derived from the differential pressure measurements of the 3-D probe. Figure 6 is an example of the temperature profile, the yaw angle, and the pitch angle (for the 3-D probe only) along chords 1 and 2 for heated flow conditions. The temperature inside the exhaust duct was less than 400 K for a heat input of 2 MW. For a heated experiment, the typical temperature profile had a range of 15 K or less. The temperature was lowest near the probe access ports at *r* = -75 cm due to fresh air leaking into the duct. Moving further into the duct, the temperature increased to reach a plateau near the center of the duct. Yaw angles were the greatest near the walls, especially near the wall containing the probe access port. Yaw angles at the walls were less than 15°. Similarly, the greatest pitch angles were observed near the walls and were less than 6°.

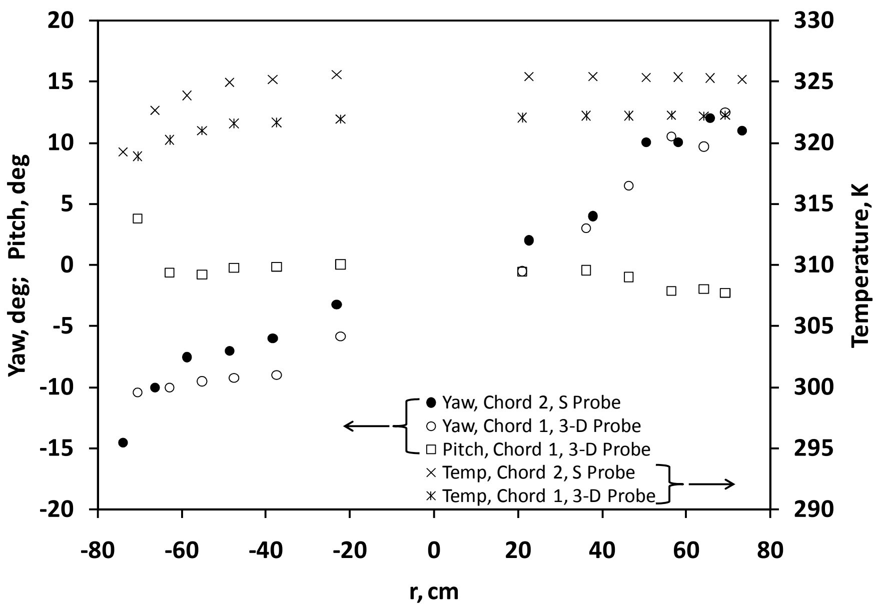

Figure 6. Example profiles of gas temperature and flow angles with respect to the velocity probe.

Measured and Computed Velocity Profiles

Beginning with cold flow conditions, velocity traverses were first performed in the large exhaust hood with a uniform spacing of 2.54 cm. CFD results were computed for this case. The measured and computed velocity profiles are shown in Figure 7. Each velocity measured at the probe is plotted normalized by the corresponding velocity measured at the annubar. The CFD velocity is scaled so that the average CFD velocity equals the average measured velocity. Both the CFD results and the measured profiles exhibited similar trends. On chord 1, both the CFD and measured profiles are nearly symmetric. In contrast, the measured profile is flat outside the boundary layer while the CFD profile decreases at smaller radii, reaching a local minimum near the center of the duct. On chord 2, both the CFD and measured profiles are skewed so that the velocity peaks on the far side just prior to the boundary layer. However, the CFD predicts a much more pronounced velocity peak than the measurements. Although velocity differences were as large as 10 %, the CFD is in good qualitative agreement (*i.e.*, similar velocity profile) with the measurements. In future work we hope to improve the CFD predictions by using more sophisticated turbulence models.

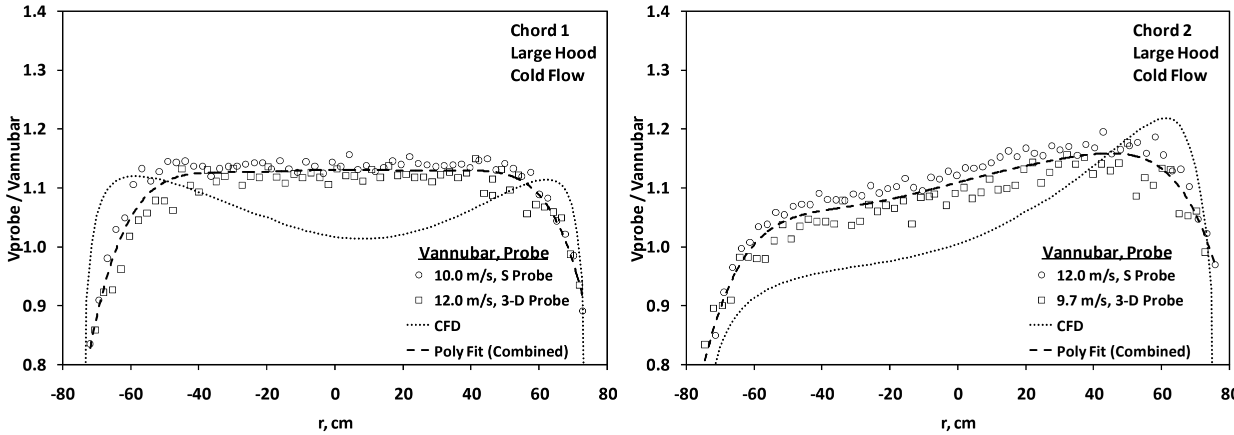

Figure 7. Velocity profiles on chord 1 and chord 2 for cold flow conditions in the large exhaust duct.

Both the S probe and the 3-D probe recover the same general shape of the velocity profiles. A least-squares polynomial fit of the data from both probes is plotted in Figure 7. Measurements from the S probe fall above the fit, while measurements from the 3-D probe fall below the fit. This is consistent for both chords and suggests a bias between the two measurements. An uncertainty propagation was performed to estimate the combined uncertainty of the velocity computed from the measurements at a single location along the chord. Initial estimates of the relative expanded (95 % confidence interval) uncertainty of the velocity inferred from the S probe and 3-D probe measurements were 1.0 % and 4.1 %, respectively. The standard deviation of the residuals of the data to the fit is 0.019 on chord 1 and 0.022 on chord 2. This represents a relative agreement of approximately 4.0 %, for a 95 % confidence interval, between the measurements and the least-squares fits. Using the fits for reference, this also represents good agreement between the measurements from the two probe types when normalized by the annubar velocity.

Velocity traverses with uniform spacing were repeated for conditions of heated flows (1 MW and 2 MW) with the natural-gas burner placed at the southwest (SW) quadrant of the footprint of the large exhaust hood. Figure 8 shows that the general shape of the profiles was consistent with the least-squares fit for the cold flow. The burner was relocated to the center (C) of the exhaust hood and traverses were repeated but for 12 equal area positions instead of the uniform spacing. The profiles were excluded from the figures for clarity, but were also similar to the cold flow profiles. These initial observations suggest that the addition of heat to the flow and the change of location of the heat source did not produce significant change in the velocity profiles for the large exhaust hood.

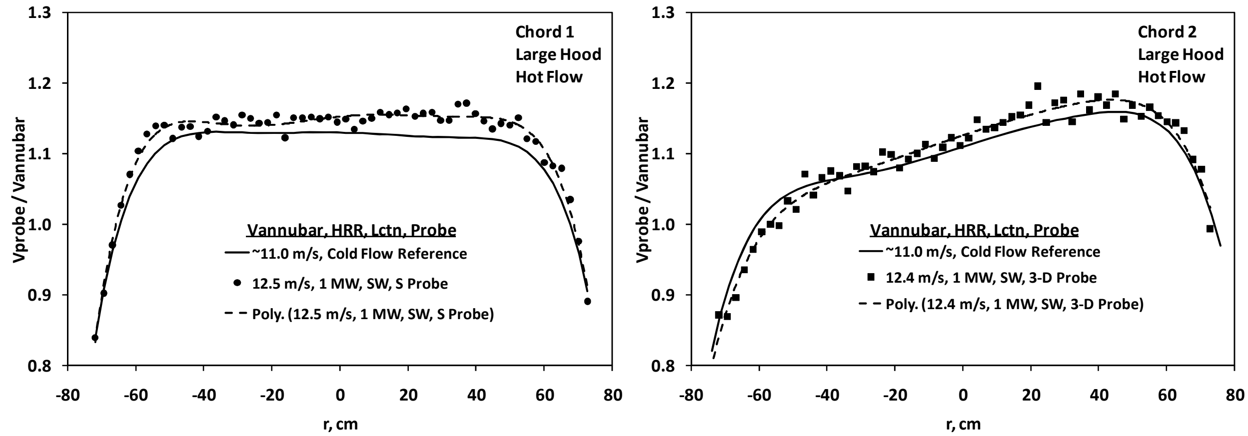

Figure 8. Velocity profiles on chord 1 and chord 2 for heated flow conditions in the large exhaust hood.

The conditions at the inlet to the exhaust duct were changed by moving the natural-gas burner to the medium exhaust hood. Velocity traverses were conducted for 12 equal area positions on each chord, Figure 9. The least-squares fit from the cold-flow velocity traverses with 2.54 cm spacing for the large hood are plotted for comparison. The flow profile for the heated flow in the medium exhaust hood is distinctly different when compared to the flow profile in the large exhaust hood. On chord 1, there appears to be some change in the profile due to flow magnitude. These observations reveal how the flow profiles are sensitive to parameters such as choice of exhaust hood, flow settings, and possibly heat input.

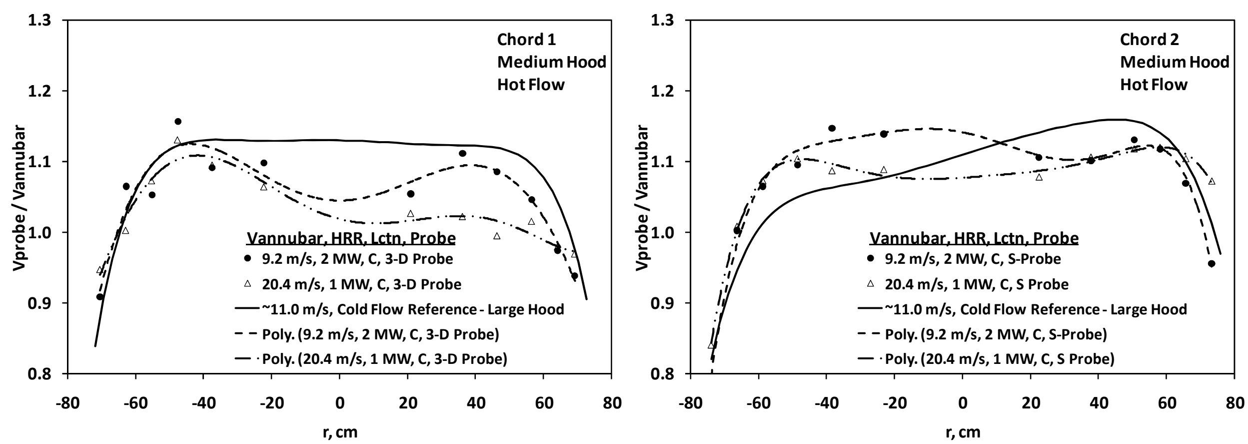

Figure 9. Velocity profiles for the medium sized exhaust hood for heated flow conditions. The least-squares fit from the large exhaust hood, cold flow condition, is plotted for comparison.

At a later date, velocity traverses were repeated, but with two S probes - one on chord 1 and one on chord 2. For significant changes in experimental conditions, such as the transition from the large exhaust hood to the medium exhaust hood or cold flow to heated flow, coarse surveys were conducted to assess the amount of off-axis flow. When the estimated change in average velocity due to off-axis flow was less than 0.5 %, the velocity traverses were conducted following EPA Method 2, using 48 equal area positions (24 on each chord). Otherwise, EPA Method 2G was followed to measure yaw angle and the near-axial velocity; 40 equal area positions (20 on each chord) were sampled. The reduced spatial sampling resolution allowed more experiments to be performed. This resulted in a greater number of repeat measurements and an expanded range of experimental conditions.

Like the first series of experiments, this series began with cold flow conditions in the large exhaust hood. Off-axis flow was not significant for the cold flow and it was not significant for the heated flow conditions when the burner was located in the southwest quadrant of the exhaust hood. Cold-flow velocity profiles are shown in Figure 10. Each velocity measured at the probe is plotted normalized by the average velocity measured at the annubar. The annubar average velocity is computed for the duration of traverse. The velocity profiles are consistent with those from the first series for the cold flow conditions. Least-squares polynomial fits are plotted for the repeat measurements. In the region between the boundary layers, the velocity ratio moves closer to unity with increasing flow magnitude. When 1 MW and 2 MW of thermal energy were added to the flow, the shape of the velocity profiles, Figure 11, remained consistent with the cold flow profiles. Moving the natural-gas burner from the southwest quadrant to the center of the exhaust duct did not have a significant effect on the velocity profile, but the amount of off-axis flow increased. Hence, Method 2G was followed for experiments with the natural-gas burner centered under the exhaust hood.

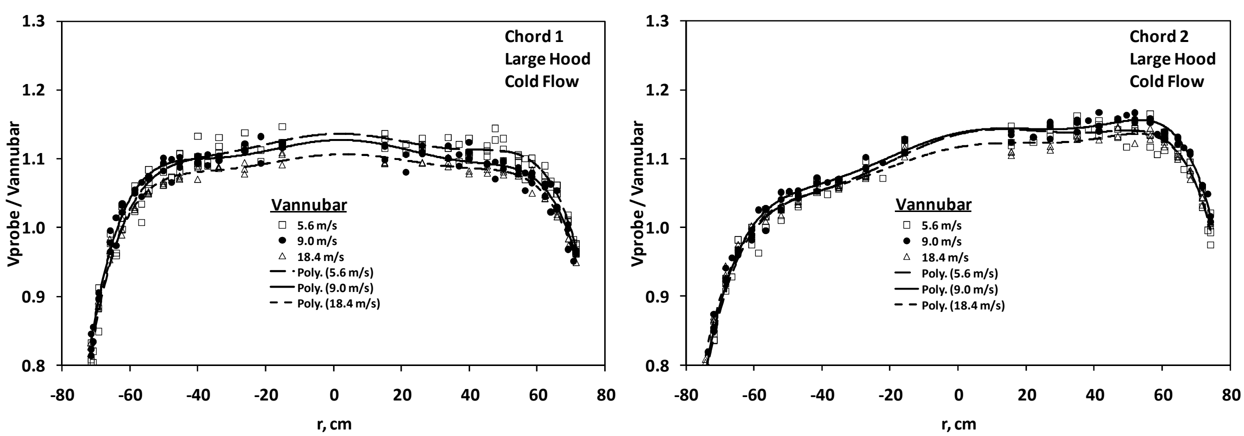

Figure 10. Velocity profiles for cold flow conditions in the large exhaust hood. S probes were used on both chords, and sample locations correspond to equal area positions.

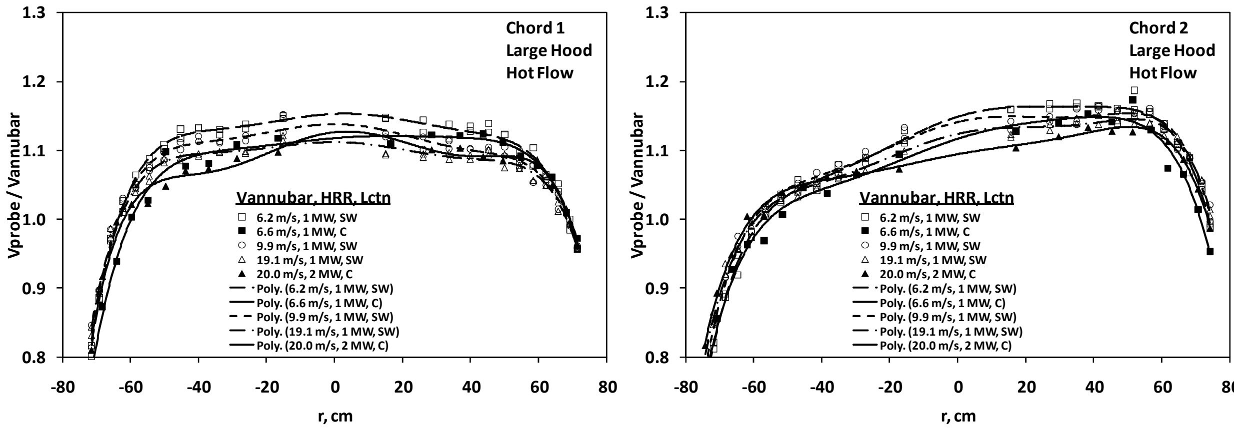

Figure 11. Velocity profiles for heated flow conditions in the large exhaust hood.

Figure 12 shows the velocity profiles when the exhaust inlet conditions were changed by moving the natural-gas burner to the center of the medium exhaust hood. Method 2G was followed for all traverses using the medium hood to measure yaw angle and near-axial velocity. For the cold flow conditions, the flow profile on chord 1 is not symmetric while the profile on chord 2 exhibits greater symmetry. This is opposite to the flow behavior observed when flow originates from the large exhaust duct. Velocity profiles for heated flow conditions are shown in Figure 13. The addition of heat had little effect to the chord 1 flow profile at the high velocity but it appears to have increased the symmetry for the low velocity flow. A decrease in symmetry also occurred on chord 2 when heat was added. These observations suggest that the resulting flow profiles for flow originating from the medium exhaust hood are sensitive to flow magnitude and heat input.

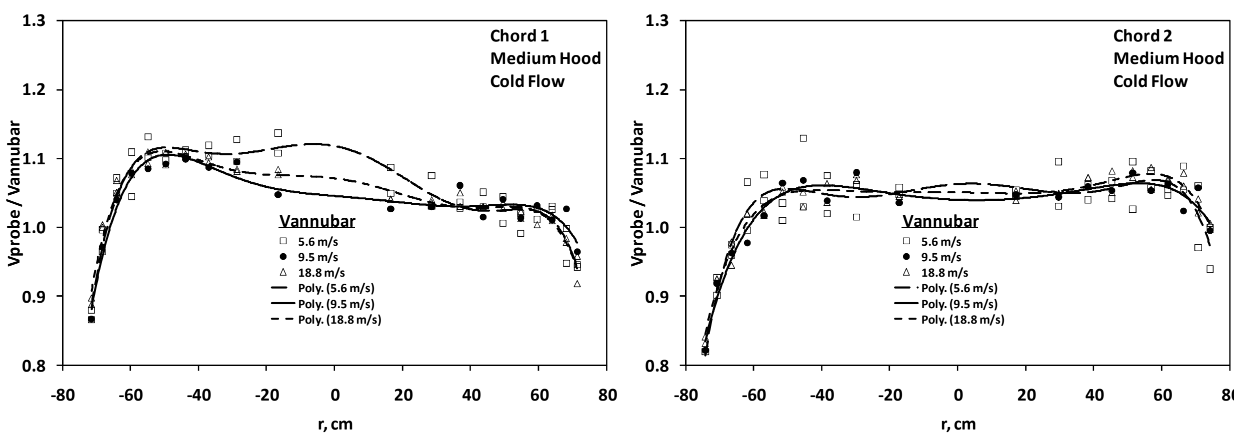

Figure 12. Velocity profiles for cold flow conditions in the medium exhaust hood. S probes were used on both chords, and sample locations correspond to equal area positions.

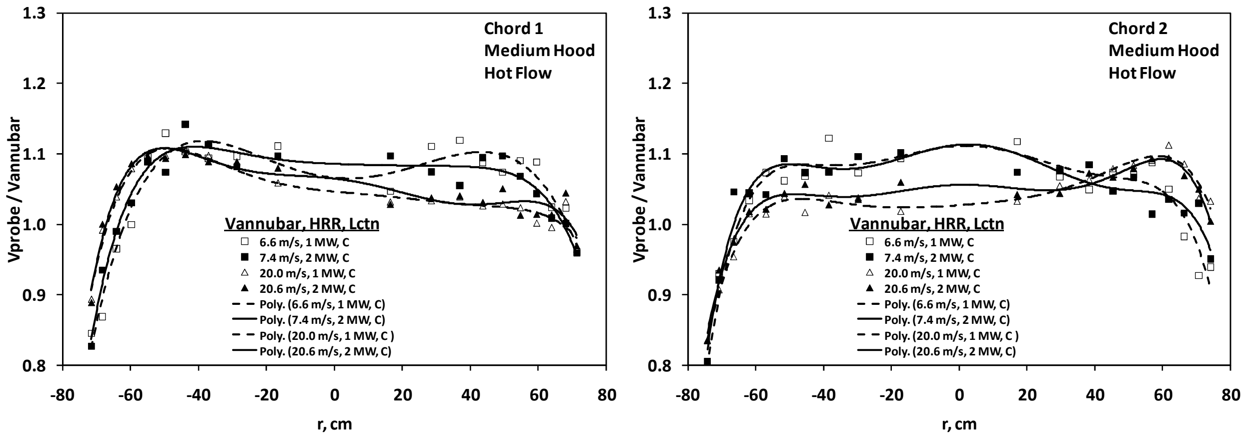

Figure 13. Velocity profiles for heated flow conditions in the medium exhaust hood.

CONCLUSIONS

Velocity traverses were conducted across two perpendicular chords in the exhaust duct of the NIST Large Fire Laboratory using S probes and 3-D probes. For cold flow conditions velocity profiles were also determined by CFD modeling. Traverses for cold flow conditions were used to establish reference flow profiles. Velocity profiles determined from CFD simulations showed good qualitative agreement for cold flow conditions. Based on CFD calculations the error attributed to traversing the measurement plane along only 2 chords (azimuthal discretization) was estimated to be almost 1 %. Flow inlet conditions were varied by changing heat input, burner location, and exhaust hood. Qualitative analysis of the flow profiles reveals that significant asymmetry exists in the duct flow that originates from the large exhaust hood, and it is consistent for all conditions. Velocity profiles for flow originating from the large exhaust hood were not particularly sensitive to the addition of heat to the flow or to the change of location of the heat source. A similar analysis of velocity profiles of the duct flow originating from the medium hood shows more flow symmetry. However, the shape of the velocity profiles, including symmetry, appears to be sensitive to the addition of heat and sensitive to the magnitude of the flow when heat is added.

The good qualitative agreement between the simulations and experiments demonstrates that CFD is a promising tool for designing better flow and measurement configurations that are less sensitive to normal operational changes in the exhaust system. Ultimately, the flow profiles presented here will be used to compute the average velocity in the exhaust duct. Realizing that the computations will include error due to the discrete measurements, the CFD results will also be used to reduce this error by evaluating the various methods of computing average velocity in a stack or duct.

References

[1] Bryant, R. A.; Ohlemiller, T. J.; Johnsson, E. L.; Hamins, A.; Grove, B. S.; Guthrie, W. F.; Maranghides, A.; Mulholland, G. W. *The NIST 3 Megawatt Quantitative Heat Release Rate Facility*; NIST Special Publication 1007; National Institute of Standards and Technology: Gaithersburg, MD, 2003.

[2] Hirsh, C., *Numerical Computation of Internal and External Flows, Volume 1, Fundementals of Numerical Discretization*, John Wiley & Sons: New York. 1988.

[3] Kato, M. and Launder, B., E., *The Modeling of Turbulent Flow Around Stationary and Vibrating Square Cylinders*, Proceedings 9th Symposium on Turbulent Shear Flows, Kyoto, August 1993, pp. 10.4.1 – 10.4.6.

[4] *Sample and Velocity Traverses for Stationary Sources*; EPA Method 1; Environmental Protection Agency: 2000.

[5] *Determination of Stack Gas Velocity and Volumetric Flow Rate (Type S Pitot Tube)*; EPA Method 2; 2000.

[6] *Determination of Stack Gas Velocity and Volumetric Flow Rate with Two-Dimensional Probes*; EPA Method 2G; 2007.